

Galaxy Activity, Torus and Outflow Survey (GATOS) X: Molecular gas clumpiness under the influence of AGN

Federico Esposito¹, Almudena Alonso-Herrero², Santiago García-Burillo¹, Ismael García-Bernet², Françoise Combes^{3,4}, Richard Davies⁵, Enrique Lopez-Rodriguez^{6,7}, Omaira González-Martín⁸, Cristina Ramos Almeida^{9,10}, Anelise Audibert^{9,10}, Erin K. S. Hicks¹¹, Miguel Querejeta¹, Claudio Ricci^{12,13}, Enrica Bellocchi^{14,15}, Peter Boorman¹⁶, Andrew J. Bunker¹⁷, Steph Campbell¹⁸, Daniel E. Delaney¹¹, Tanio Díaz-Santos^{19,20}, Donaji Esparza-Arredondo⁸, Sebastian Hönig²¹, Álvaro Labiano Ortega²², Nancy A. Levenson²³, Chris Packham²⁴, Miguel Pereira-Santaella²⁵, Rogemar A. Riffel^{26,27}, Dimitra Rigopoulou^{17,19}, David J. Rosario¹⁸, Antonio Usero¹, and Lulu Zhang²¹

(Affiliations can be found after the references)

Received XXX; accepted YYY

ABSTRACT

The distribution of molecular gas on small scales regulates star formation and the growth of supermassive black holes in galaxy centers, yet the role of active galactic nuclei (AGN) feedback in shaping this distribution remains poorly constrained. We investigate how AGN influence the small-scale structure of molecular gas in galaxy centers, by measuring the clumpiness of CO(3 – 2) emission observed with the Atacama Large Millimeter/submillimeter Array (ALMA) in the nuclear regions (50 – 200 pc from the AGN) of 16 nearby Seyfert galaxies from the Galaxy Activity, Torus, and Outflow Survey (GATOS). To quantify clumpiness, we apply three different methods: (1) the median of the pixel-by-pixel contrast between the original and smoothed maps; (2) the ratio of the total excess flux to the total flux, after subtracting the background smoothed emission; and (3) the fraction of total flux coming from clumpy regions, interpreted as the mass fraction in clumps. We find a negative correlation between molecular gas clumpiness and AGN X-ray luminosity (L_X), suggesting that higher AGN activity is associated with smoother gas distributions. All methods reveal a turnover in this relation around $L_X = 10^{42}$ erg s⁻¹, possibly indicating a threshold above which AGN feedback becomes efficient at dispersing dense molecular structures and suppressing future star formation. Our findings provide new observational evidence that AGN feedback can smooth out dense gas structures in galaxy centers.

Key words. Galaxies: active – Galaxies: nuclei – Galaxies: ISM – ISM: structure – ISM: evolution

1. Introduction

Active galactic nuclei (AGN) are powerful sources of energy and momentum that can significantly impact the interstellar medium (ISM) of their host galaxies. The feedback processes driven by AGN, including both radiative and mechanical effects, play a crucial role in shaping the gas distribution, star formation, and overall evolution of galaxies (Fabian 2012; Kormendy & Ho 2013; Heckman & Best 2014; Morganti 2017; Harrison et al. 2018). Deciphering the mechanisms by which AGN feedback affects the ISM and drives galaxy evolution is one of the major challenges in modern astrophysics (see Harrison & Ramos Almeida 2024, for a recent review).

Within a galaxy, molecular gas can organize into Giant Molecular Clouds (GMCs), with typical masses $M_{\text{GMC}} \sim 10^4 - 10^6 M_{\odot}$ and sizes of $\sim 10 - 50$ pc (Solomon et al. 1987; Omont 2007; Fukui & Kawamura 2010; Heyer & Dame 2015; Chevance et al. 2020, 2023). Such clouds are sufficiently massive and dense that their self-gravity tends to drive gravitational collapse. However, GMCs can achieve a quasi-stable state because other internal forces – mainly magnetic pressure and turbulent motions – provide support that counteracts collapse (McKee & Ostriker 2007; Crutcher 2012). Within them there exists a complex hierarchical structure of smaller and smaller high density structures (Elmegreen & Falgarone 1996; Federrath & Klessen 2012; Elia et al. 2018; Buck et al. 2022), which are thought to be the sites

of star formation (Bergin & Tafalla 2007; Heyer & Dame 2015; Massi et al. 2019).

AGN-driven radiation, winds, jets, and cosmic rays can further compress, evaporate, or disperse the gas (Pier & Voit 1995; Schartmann et al. 2011; Namekata et al. 2014; Pozzi et al. 2017; Vallini et al. 2017; Mingozi et al. 2018; Circosta et al. 2021; Gabici 2022; Bertola et al. 2024; Koutsoumpou et al. 2025), and although there are hints of positive feedback (e.g. Maiolino et al. 2017; Bessiere & Ramos Almeida 2022; Mercedes-Feliz et al. 2023), we mostly observe molecular gas depletion in the central regions of active galaxies (Sabatini et al. 2018; Rosario et al. 2019; Ellison et al. 2021; García-Burillo et al. 2021, 2024). Among the clearest signatures of AGN impact on the host ISM, García-Burillo et al. (2021, 2024) reported a systematic deficit in the central concentration of cold molecular gas in AGN-host galaxies, quantified through the concentration index $\log(\Sigma_{50}/\Sigma_{200})$, where Σ_{50} and Σ_{200} are the average CO surface densities within circular apertures of 50 pc and 200 pc radii, respectively. They found that this concentration index shows a turnover as a function of AGN X-ray luminosity, with a change around $L_X(2 - 10 \text{ keV}) \sim 10^{41.5}$ erg s⁻¹. While the concentration index quantifies how centrally peaked the gas distribution is, it does not capture the small-scale structure within the nuclear region. In this work, we focus on the clumpiness of the molecular gas, a property that reflects how fragmented or structured the emission is within the nuclear region.

Molecular gas clumpiness, characterised by an irregular and dense distribution, can serve as an indirect measure of star formation activity, as the most clumpy regions are where the gravitational collapse leads to the formation of new stars (Krumholz 2014; Krumholz et al. 2019). Understanding the potential role that AGN feedback plays in shaping the molecular gas clumpiness of their host galaxies is crucial for assessing how AGN can regulate star formation and the evolution of galaxy centers. To this end, this work is part of the Galaxy Activity, Torus, and Outflow Survey (GATOS¹, García-Burillo et al. 2021; Alonso-Herrero et al. 2021; García-Bernete et al. 2024a,b; Zhang et al. 2024; Poitevineau et al. 2025; Fuller et al. 2025), an ongoing effort to study the properties of AGN, of the dusty molecular tori, and the AGN interaction with the host galaxy in local Seyfert galaxies using high resolution observations.

The paper is structured as follows: in Section 2 we introduce the sample of galaxies, in Section 3 we describe the methods for measuring clumpiness, and the statistical tools employed in our analysis. Section 4 presents the results of our analysis, and in Section 5 we discuss the implications of our findings in the context of AGN feedback on the molecular gas. Finally, we summarise our conclusions in Section 6.

2. Sample description

The initial sample consists of 19 nearby (luminosity distance $D_L < 28$ Mpc) AGNs, combining the NUGA sample (Nuclei of Galaxies, Combes et al. 2019; Audibert et al. 2019, 2021) with the core sample of GATOS galaxies presented in García-Burillo et al. (2021). The GATOS core sample was selected from the 70 month *Swift*-BAT all-sky hard-X ray survey (Baumgartner et al. 2013) with distances $D_L < 28$ Mpc and luminosities $L(14 - 150 \text{ keV}) \geq 10^{42} \text{ erg s}^{-1}$. The CO(3 - 2) data used here were analysed in detail by García-Burillo et al. (2021), where moment maps and kinematic modelling are discussed. All galaxies have CO(3 - 2) emission observed with the Atacama Large Millimeter/submillimeter Array (ALMA) Band 7, covering a field of view of $17''$, and spatial resolutions ranging from $0.08''$ to $0.2''$, corresponding to a physical size range of 4 - 16 pc.

Inclinations and position angles of the targets are taken from García-Burillo et al. (2021), which reported the results of a kinematical analysis performed with the kinometry software (Krajinović et al. 2006). Since our goal is to study the clumpiness of the molecular gas, we have decided to discard the highly inclined ($i > 75^\circ$) galaxies from the original sample. This decision was made to avoid severe projection effects, as high inclination makes it more likely for the line of sight to intersect multiple layers of clumps and diffuse gas. This selection results in a sample of 16 galaxies, all with inclinations $i < 60^\circ$. Their intrinsic 2 - 10 keV luminosities span from 10^{39} to $10^{43.5} \text{ erg s}^{-1}$, and their Eddington ratios, $\lambda_{\text{Edd}} \equiv L_{\text{AGN}}/L_{\text{Edd}}$, range from -6.4 to -0.7 in logarithmic scale. Table A.1 lists the basic properties of the galaxies analysed in this study, and Figure A.3 presents an atlas of their CO(3 - 2) emission.

The sensitivity of the CO(3 - 2) maps ranges from 6 to 28 mJy km s⁻¹ beam⁻¹. We checked whether this sensitivity correlates with the luminosity distance of the galaxies, and found no such trend (see Figure A.1). To express these values in terms of molecular mass surface density, we adopted reasonable conversion factors: first from CO(3 - 2) to CO(1 - 0) (r_{31}), and then from CO(1 - 0) to molecular mass via the CO-to-H₂ conversion factor (X_{CO}). We explored two extreme cases. The first

assumes $r_{31} = 0.7$, the average value measured by Israel (2020) in 126 galaxy centers, combined with the standard Milky Way disk value $X_{\text{CO}} = 2 \times 10^{20} \text{ mol cm}^{-2} (\text{K km s}^{-1})^{-1}$ (Bolatto et al. 2013). The second adopts $r_{31} = 2.9$, as measured at the AGN position of NGC 1068 by Viti et al. (2014), coupled with the recommended value for the central region ($R < 500$ pc) of the Milky Way, $X_{\text{CO}} = 0.5 \times 10^{20} \text{ mol cm}^{-2} (\text{K km s}^{-1})^{-1}$ (Bolatto et al. 2013). With the first set of parameters, the resulting sensitivities span 23 - 381 M_⊙ pc⁻², while with the second they range from 1 to 23 M_⊙ pc⁻² (see Figure A.2). The achieved sensitivities are generally comparable to, or lower than, the average surface density of GMCs (170 M_⊙ pc⁻², McKee & Ostriker 2007), and in most cases sufficient to detect individual GMCs within a single ALMA beam at the 3σ level.

3. Data analysis

3.1. Identifying the clumps

To visualise and measure the clumpiness of the molecular gas, we chose the clumpiness parameter described by Conzelice (2003) among those available in the literature. While Conzelice (2003) originally estimated clumpiness (S), together with concentration (C) and asymmetry (A), from optical images tracing stellar light in entire galaxies — the so-called CAS parameters — this method has since been applied to ALMA CO(2 - 1) observations by Yamamoto et al. (2025), using data from the Physics at High Angular resolution in Nearby Galaxies (PHANGS Leroy et al. 2021) survey.

The method involves smoothing the original observation and subtracting the smoothed map (B , for blurred) from the original intensity map (I). This results in an $I - B$ residual map, which highlights only the high-spatial frequency components of the original map. Negative pixels (where $I - B < 0$) are set to zero. The clumpiness parameter (S) calculated by Conzelice (2003) is then normalised by the original intensity, $S = (I - B)/I$, so that it has a value between zero (indicating smooth emission, with no clumps) and one (indicating high clumpiness). In this work, we follow the procedure outlined in Conzelice (2003) to identify the clumps, defined as the pixels or contiguous regions where $I - B > 0$. We then apply three different methods to quantify the clumpiness of the gas, as described in the following sections. Before performing any analysis, we first smooth all the CO maps to a common physical resolution of 16 pc, corresponding to the largest ALMA beam in the sample.

3.2. Smoothing CO(3-2) maps

A critical factor of the Conzelice (2003) procedure is the size of the smoothing kernel. Ideally, we want the full width at half maximum (FWHM) of the kernel to be larger than the spatial resolution but smaller than the aperture we are considering. Moreover, we expect the largest GMCs to have sizes of $\lesssim 100$ pc (see, e.g., García et al. 2014), so smoothing over this size would result in blending several GMCs and diluting the high-density gas. Therefore, we use smoothing kernels with FWHM between 20 and 100 pc in the following analysis. We will discuss the implications of different kernel sizes in Section 5.

An example of the full procedure can be seen in the four panels of Figure 1 for the galaxy NGC 3227. We first smooth the native-resolution CO(3 - 2) emission map (*first panel*) with a 16-pc Gaussian kernel to bring all galaxies to a common physical resolution (*second panel*). This map is then smoothed again with a larger Gaussian kernel (50 pc in Figure 1), producing a

¹ <https://gatos.myportfolio.com>

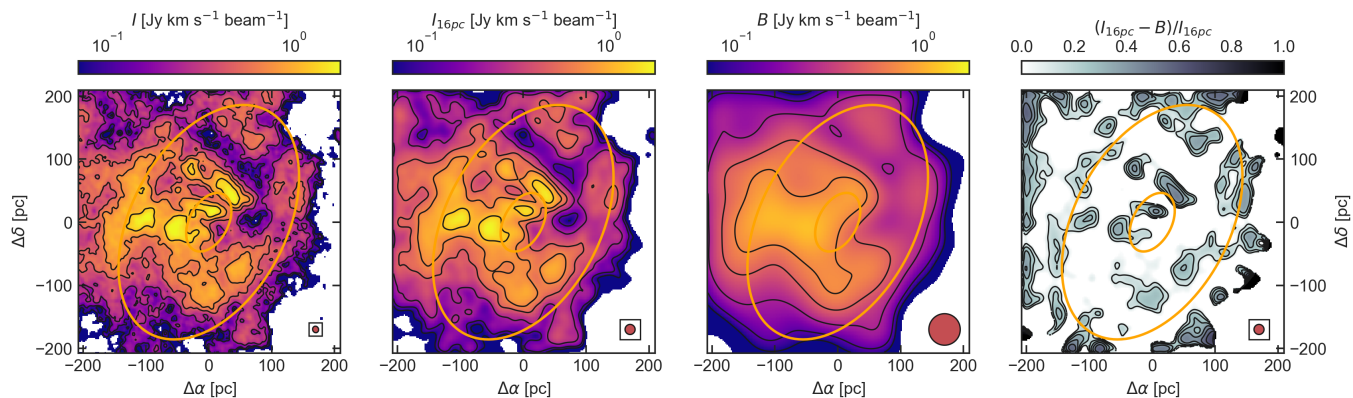


Fig. 1: ALMA observations of the CO(3 – 2) emission in the target galaxy NGC 3227 and the clumpiness computation applied within a $400 \text{ pc} \times 400 \text{ pc}$ box around the AGN. *First panel*: CO(3 – 2) emission at native resolution ($10.5 \times 9.4 \text{ pc}$), with contours at $(3, 5, 10, 20, 30, 50) \times \sigma$. *Second panel*: CO(3 – 2) emission smoothed to a common physical resolution of 16 pc, using contours at the same σ levels. *Third panel*: CO(3 – 2) emission further smoothed with a Gaussian kernel of FWHM 50 pc, with the same contour levels. *Fourth panel*: clumpiness map computed with Method #1 (see Section 3.3), with contours every 0.1 from 0 to 1. In all panels, the two ellipses correspond to circles of 50 and 200 pc radius in the galaxy plane, projected onto the sky. The red ellipse within a square in the bottom right of each panel shows the native ALMA beam ($10.5 \times 9.4 \text{ pc}$ in this case).

version that traces the average gas distribution over the corresponding spatial scale (*third panel*). We subtract this smoothed map from the 16-pc map and retain only the pixels with positive residuals (*fourth panel*; see details on how clumpiness is computed below). This procedure highlights the regions where the emission is significantly more concentrated than the surrounding gas distribution, identifying candidate clumps.

3.3. Measuring nuclear and circumnuclear clumpiness

In contrast to distant quasars (see, e.g., Maiolino et al. 2012; Genzel et al. 2014; Carniani et al. 2017; Bischetti et al. 2019), nearby AGNs are generally found to primarily affect their host galaxies within the central kiloparsec, mainly due to their lower luminosities and outflow energetics (see, e.g., Querejeta et al. 2016b; Fluetsch et al. 2019; Esposito et al. 2022, 2024a,b; García-Bernete et al. 2021; Ramos Almeida et al. 2022; García-Burillo et al. 2021, 2024). In this work, we follow García-Burillo et al. (2021, 2024) in defining two concentric regions centred on the AGN position (based on the ALMA continuum peak, see García-Burillo et al. 2021), with radii of 50 pc and 200 pc in the plane of the galaxy. These scales were previously adopted to compute the cold molecular gas concentration index ($\text{CCI} \equiv \log(\Sigma_{50}/\Sigma_{200})$). We use inclinations and position angles to project these two circles onto the plane of the galaxy. An example of this can be seen in Figure 1, where the two ellipses are drawn on top of the CO(3 – 2) emission map. We explore three different methods for measuring the clumpiness within the 50-pc and 200-pc apertures.

3.3.1. Method #1: median clumpiness

The first method follows that of Conzelmann (2003): we calculate the clumpiness as $(I - B)/I$ pixel by pixel, setting negative pixels to zero, as shown in the fourth panel of Figure 1. We then take the median value of the clumpiness within the two apertures, referring to this method as "Method #1: median clumpiness". To estimate the errors, we use the 1σ distance from the median values. This method provides a clumpiness value that can be compared with other studies (e.g. Conzelmann 2003; Yamamoto et al.

2025). However, high clumpiness values tend to identify regions with higher contrast, especially in the outskirts of the CO emission, rather than dense or massive clumps, as visible in Figure 1. For this reason, we sought alternative methods to estimate the fraction of gas in clumps.

3.3.2. Method #2: $\Sigma_{I-B}/\Sigma_{\text{tot}}$

The second method is similar to Method #1 in principle, as it calculates the clumpiness as $(I - B)/I$. However, instead of computing it pixel by pixel and then taking the median value, we separately sum the $I - B$ and I values within the apertures and then divide them. We call this method "Method #2: $\Sigma_{I-B}/\Sigma_{\text{tot}}$ ". Since CO intensity can be converted to molecular mass using a CO-to- H_2 conversion factor α_{CO} , and assuming the same α_{CO} for both the clumpy emission and the underlying smooth emission, the result of $\Sigma_{I-B}/\Sigma_{\text{tot}}$ can be interpreted as the mass fraction of gas in clumps, independent of the choice of α_{CO} . This method returns values between 0 and 1, where higher values indicate a greater contrast between clumpy and smooth gas. Since this method is analogous to aperture photometry, we use the photometric errors to estimate the uncertainties. For the ALMA observations, these are dominated by the calibration error, which can be as high as $\sim 10\%$ (Francis et al. 2020). This results in a propagated uncertainty of $\sim 17\%$.

3.3.3. Method #3: $\Sigma_{\text{clumps}}/\Sigma_{\text{tot}}$

The third method uses the condition $I - B > 0$ to identify the clumps and sums the original pixel intensities I (without subtracting the smoothed B emission) to calculate the flux of the clumps, Σ_{clumps} , within the different apertures. We then divide this by the total flux Σ_{tot} , and refer to this as "Method #3: $\Sigma_{\text{clumps}}/\Sigma_{\text{tot}}$ ". By not subtracting the smoothed emission, we aim to obtain a more direct measurement of the fraction of molecular mass in clumps. As a result, this method tends to yield systematically higher clumpiness values compared to the other two. As with the second method, we assume a $\sim 10\%$ error on the flux measurements, which propagates to a $\sim 14\%$ uncertainty.

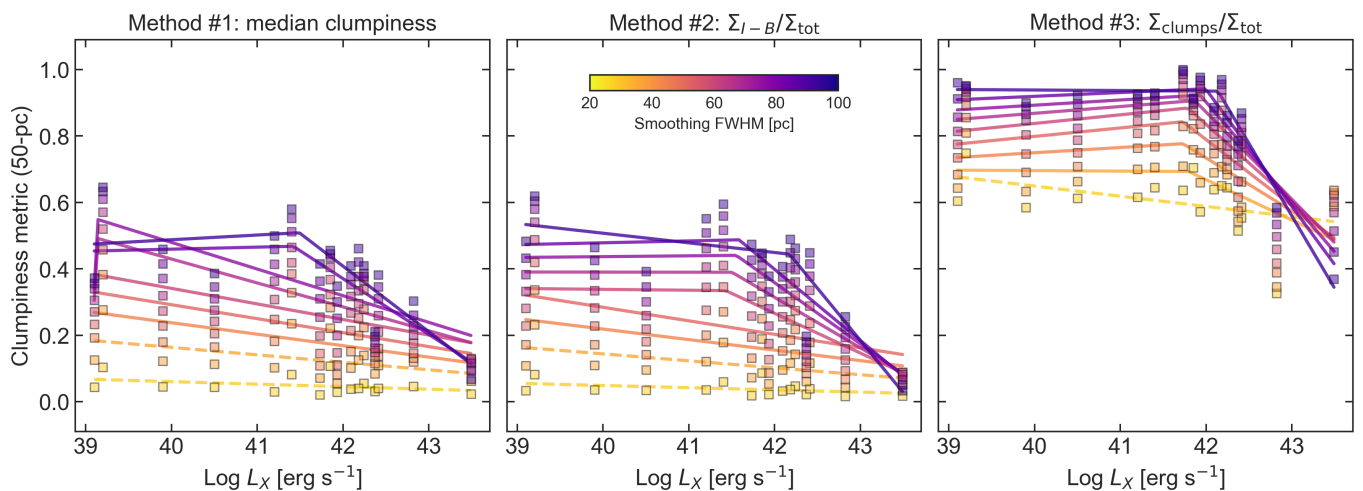


Fig. 2: Clumpiness as a function of AGN intrinsic X-ray 2 – 10 keV luminosity. Clumpiness is measured within the nuclear 50-pc-radius aperture with the three different methods described in Section 3.3 (panels left to right). Data points (square markers; nine per galaxy) are coloured according to the nine smoothing FWHM sizes adopted (see colour bar in the central panel). Coloured lines show the `pwlfit` fits to the data points, with the same colour as the fitted dataset; lines are solid where a linear fit is statistically accepted, and dashed where it is rejected (see Section 3.4).

These three methods are designed to capture complementary aspects of clumpiness, each with its own sources of systematic uncertainty. Using multiple approaches allows us to test the robustness of our results against these effects, rather than relying on a single estimator of clumpiness.

3.4. Estimating the influence of AGN on clumpiness

One of the most reliable indicators of the power of an AGN is its intrinsic 2 – 10 keV X-ray luminosity, L_X , which serves as a proxy for both radiative feedback on the ISM (through the creation of X-ray dominated regions, or XDRs; see, e.g., Maloney et al. 1996; Wolfire et al. 2022; Esposito et al. 2024b; Tadaki et al. 2025) and mechanical feedback (through the interaction of AGN winds with the host galaxy’s ISM; see, e.g., Faucher-Giguère & Quataert 2012; Ciccone et al. 2014; Nims et al. 2015; Fiore et al. 2017; Esposito et al. 2024a). We use L_X as a measure of AGN power and investigate whether there are correlations between the AGN emission and our different clumpiness measurements, considering various smoothing kernels and aperture sizes. To do this, we apply the Piecewise Linear Fitting (PWLf) algorithm using the Python package `pwlfit` (Jekel & Venter 2019), which fits continuous piecewise linear functions to the data based on a specified number of line segments. We begin by fitting both a single-segment (i.e., standard linear regression) and a two-segment model. We then perform an F-test (at the 95% confidence level) to evaluate whether the two-segment model provides a statistically significant improvement over the single-segment model. If the two-segment fit is not preferred, we adopt the single-segment model and assess the significance of its slope with a two-tailed t -test under the null hypothesis of zero slope.

For each dataset (i.e., a combination of clumpiness method, smoothing level, and aperture) where a two-segment fit is preferred, we test for the presence of a breakpoint — an L_X value where the slope changes — using two statistical techniques. First, we perform Leave-One-Out Cross-Validation (LOOCV), iteratively excluding one data point at a time to examine the distribution of breakpoints within the dataset. This helps assess whether the fit is significantly influenced by individual points.

We consider a breakpoint reliable only if the standard deviation of its LOOCV distribution is smaller than 10% of the L_X -range of the data. Second, for each validated dataset, we run 1000 Monte Carlo simulations, taking into account the data uncertainties in both axes: we assume a ± 0.15 dex uncertainty for L_X (following García-Burillo et al. 2024), while clumpiness uncertainties are described in Section 3.3. This approach allows us to statistically confirm the presence of a breakpoint and to estimate its 1σ confidence interval using Monte Carlo resampling.

4. Results

4.1. The nuclear region

Figure 2 shows the clumpiness, measured within the 50-pc-radius aperture, as a function of the X-ray luminosity, L_X , of our sample targets. Clumpiness is computed using the three methods described in Section 3.3, applying nine different smoothing levels, ranging from 20 to 100 pc in steps of 10 pc. This allows us to trace how clumpiness varies as a function of the smoothing scale.

For each smoothing level, we fit the data using the PWLf algorithm and plot the corresponding regression lines. At low smoothing levels, when the kernel size is close to the ALMA beam, the clump identification condition ($I - B > 0$) primarily selects the peaks of the clumps. As a result, Methods #1 and #2 return values close to zero with no apparent breakpoints in the fit. In contrast, Method #3 starts from a baseline value of $\Sigma_{\text{clumps}}/\Sigma_{\text{tot}} \approx 0.6$, indicating that even at the smallest smoothing scales, clumps already contribute approximately 60% of the CO emission. In addition, Method #3 already shows a statistically significant breakpoint at $L_X \sim 10^{41.8}$ erg s $^{-1}$ emerging from smoothing scales as small as 30 pc.

Up to a smoothing scale of 50 pc, the data show a significant ($p < 0.05$), weak ($r^2 < 0.4$) anti-correlation between L_X and clumpiness for Methods #1 and #2. As the smoothing level increases, a two-segment trend emerges also for these methods, with a relatively flat trend at the lowest luminosities, followed by a steep decline. The breakpoint in these cases typically falls

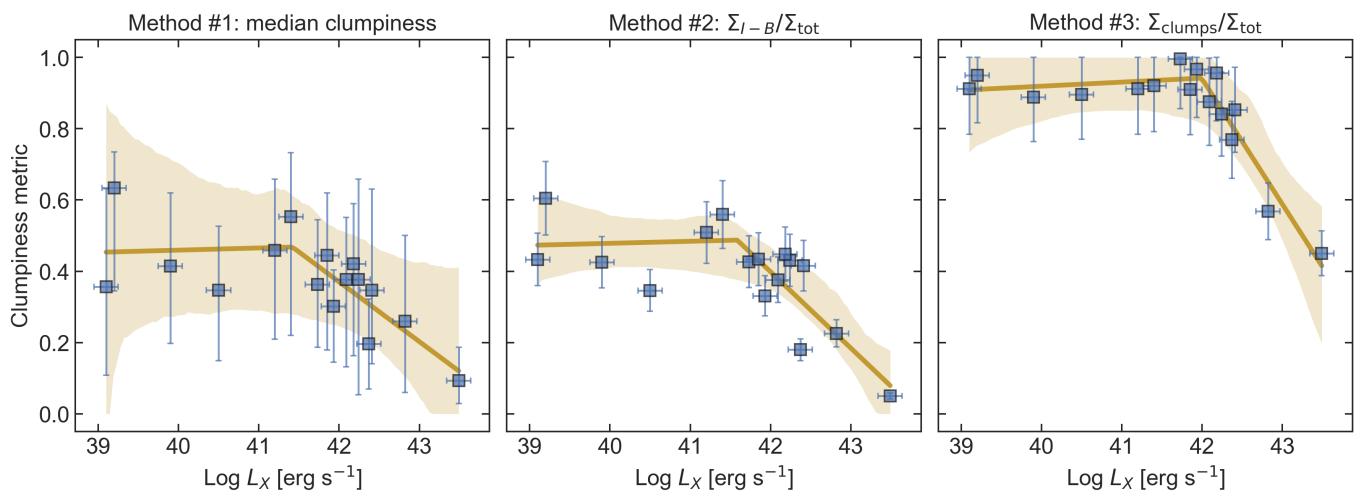


Fig. 3: Clumpiness as a function of AGN X-ray luminosity. Clumpiness is measured within the nuclear 50-pc-radius aperture with the three different methods described in Section 3.3 (panels left to right). Data points are shown as blue square markers with error bars, computed for a smoothing kernel FWHM of 90 pc. The broken orange lines indicate the pwlf fits to the data, and the shaded regions show the corresponding 95% confidence intervals.

around $L_X \sim 10^{41.5}$ erg s $^{-1}$. The exact smoothing level required to reveal a significant breakpoint depends on the method used: for Method #3, the trend appears at 30 pc; for Method #2, at 60 pc; and for Method #1, at 90 pc.

From a smoothing level of 90 pc, a two-segment fit appears for every method. Figure 3 shows the data points for this smoothing level, including error bars, the pwlf lines, and the 95% confidence interval from Monte Carlo simulations. For Method #1, the LOOCV algorithm finds a high standard deviation (30% of the L_X range), indicating that the exact position of the L_X breakpoint is not well constrained and should be treated with caution. This is further illustrated in Figure 2, where at smoothing scales of 70 and 80 pc, the breakpoint appears at very low $L_X \sim 10^{39}$ erg s $^{-1}$ — probably an artifact of the fitting process — before shifting to higher L_X values at larger smoothing scales. The broad confidence interval in Figure 3 further reflects this uncertainty. In contrast, for Methods #2 and #3, the LOOCV validates the breakpoints, with standard deviations of 7% and 1% of the L_X range, respectively, yielding $\log(L_X/\text{erg s}^{-1})_{\text{break}} = 41.99^{+0.44}_{-0.62}$ and $42.03^{+0.32}_{-0.34}$.

It is interesting to note that, for both Method #2 and #3, the breakpoint position shifts to higher X-ray luminosity values as we increase the smoothing: at 80-pc smoothing, we find the breakpoints at $\log(L_X/\text{erg s}^{-1})_{\text{break}} = 41.76^{+0.60}_{-0.45}$ and $41.92^{+0.30}_{-0.36}$, respectively for Methods #2 and #3, while at 100-pc smoothing we find them at $\log(L_X/\text{erg s}^{-1}) = 42.04^{+0.49}_{-0.62}$ and $42.12^{+0.32}_{-0.33}$. Considering only Methods #2 and #3, we find that the breakpoints are compatible with each other, given the uncertainties, to a value of $L_X \approx 10^{42}$ erg s $^{-1}$.

Finally, we explored the relation between clumpiness and the AGN Eddington ratio, λ_{Edd} , as shown in Figure A.5. We find a similar pattern (flat regime followed by a steep decline) by using Methods #1 and #3, with breakpoints between $\lambda_{\text{Edd}} = -3$ and -2 .

4.2. The circumnuclear region

Applying the same methods to the 200-pc aperture, we find significantly decreasing linear trends without breakpoints for Methods #1 and #2. Method #3 also shows an anticorrelation between

L_X and clumpiness, but no smoothing kernel size yields a significance above 2σ (see Figure 4). Beyond physical explanations (discussed in Section 5), some targets in this aperture include regions dominated by noise or empty space (e.g., NGC 7213 and NGC 1365; see Figure A.3), which may affect the analysis. When considering only the annular region between galactocentric distances of 50 pc and 200 pc, we see less significant results, probably for the high noise present in this annular aperture (see Figure A.6).

For $L_X > 10^{41.5}$ erg s $^{-1}$, local AGNs exhibit an anticorrelation between L_X and the molecular gas concentration index, defined as the ratio of surface densities within the 50-pc and 200-pc apertures (see García-Burillo et al. 2024). To compare with these findings, we calculate the ratio of clumpiness estimates within the two apertures for each method and smoothing level. As shown in Figure A.7, with all the three methods we observe a rising trend, rather than a flat regime, followed by a decline in the clumpiness ratio as a function of L_X , with a break again around 10^{42} erg s $^{-1}$. However, substantial scatter is present, likely due to the noise in the larger 200-pc aperture.

4.3. Clumpiness vs. concentration

In Figure 5 we explore the relation between the clumpiness measured within the central 50-pc aperture and the cold molecular gas concentration index ($\text{CCI} \equiv \log(\Sigma_{50}/\Sigma_{200})$). The CCI provides a more global measure of how centrally concentrated the cold molecular gas is, while the clumpiness values in Figure 5 refer to the nuclear region alone.

With all three methods we observe a rising trend of clumpiness with increasing CCI up to $\text{CCI} \sim 0.1$, after which the relation flattens. This breakpoint value is significantly lower than the one reported by García-Burillo et al. (2024) in the CCI- L_X relation, where the transition occurs around $\text{CCI} \sim 0.5$.

In Figure A.8 we present the plot of the clumpiness ratio (measured within 50 pc divided by that within 200 pc) as a function of the CCI. In this case, all three methods reveal significant correlations, with a clear break at $\text{CCI} \sim 0.6$. This breakpoint is closer to the value found by García-Burillo et al. (2024) in the CCI- L_X relation.

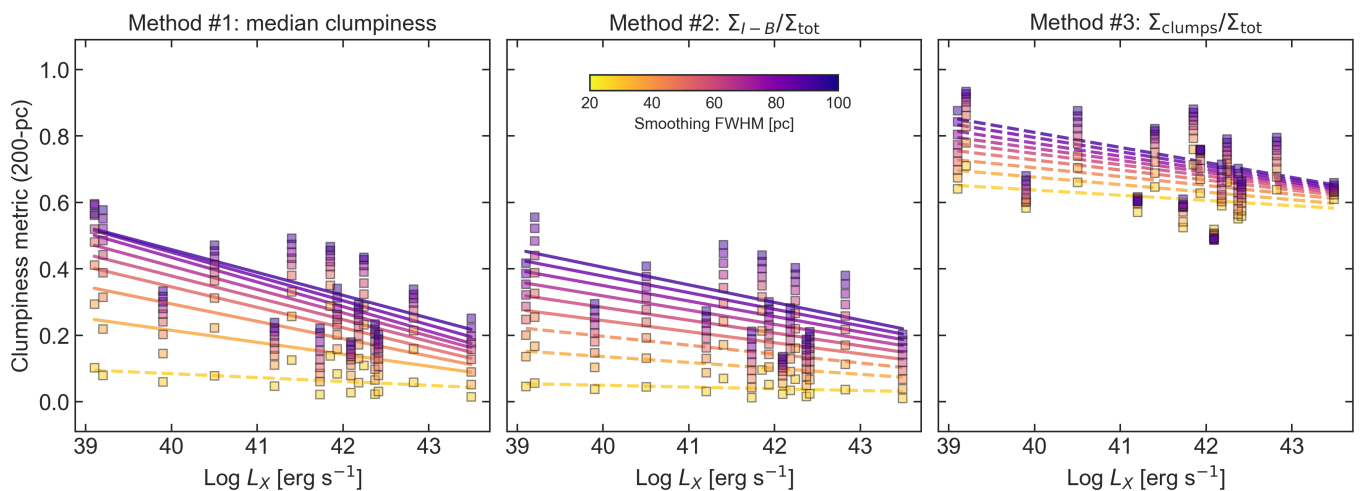


Fig. 4: Clumpiness measured within the larger 200-pc-radius aperture, plotted as a function of AGN X-ray luminosity, Panels, lines, and markers are as in Figure 2.

5. Discussion

5.1. Comparison with previous studies

Method #1 allow us to compare our measured clumpiness values with existing literature, as it is the same method originally developed by [Conselice \(2003\)](#). In their work, median clumpiness, measured from stellar light in the optical R-band, ranges from 0 for elliptical galaxies to ~ 0.7 for starburst galaxies, with data smoothed using a kernel of size $0.3 \times R(\eta = 0.2)$, where $R(\eta)$ is the Petrosian radius². The median CO(2 – 1) clumpiness in a subsample of PHANGS, mostly composed of spiral galaxies, is 0.27 ± 0.08 ([Yamamoto et al. 2025](#)), where the ALMA data (at 180 pc resolution) were smoothed with a kernel of size $0.3 \times R_e$, where the effective radius R_e of the galaxy was chosen rather than $R(\eta = 0.2)$ to better represent the spatial extent of CO(2 – 1): for example, for the PHANGS galaxy NGC 3627, $R_e \approx 66''$ while $R(\eta = 0.2) \approx 178''$ (3.6 and 9.7 kpc, respectively).

In our case, using Method #1, we find the median clumpiness in the nuclear 50-pc aperture to range from $0.08^{+0.03}_{-0.03}$ to $0.39^{+0.11}_{-0.10}$ (with the upper and lower values representing the 1σ deviation of the sample), depending on the smoothing kernel size (20 – 100 pc, see Figure 2). In the larger 200-pc aperture, these values become $0.08^{+0.07}_{-0.04}$ and $0.34^{+0.13}_{-0.12}$, respectively for 20-pc and 100-pc smoothing (see Figure 4).

These results may at first suggest that the molecular gas clumpiness in the nuclear regions of AGN-host galaxies is comparable to that observed in the discs of normal spirals (PHANGS) and much lower than the values found for the stellar emission of starburst galaxies. However, a direct comparison is not straightforward, because the measured clumpiness depends critically on the spatial scale traced by the data and on the chosen smoothing kernel. In our case, we probe only the central few hundred parsecs at a much higher resolution (16 pc), and by applying different smoothing kernels (from 20 to 100 pc) we can highlight structures of different physical sizes. In contrast, the study by [Yamamoto et al. \(2025\)](#) covers entire galaxy discs with lower resolution (180 pc), and their smoothing kernel is

² The Petrosian radius is defined as the location where the ratio of surface brightness at a radius, divided by the surface brightness within the radius, reaches some value η ([Petrosian 1976](#)).

several kpc, making it more sensitive to large-scale molecular complexes.

5.2. Clumpiness as a function of X-ray luminosity

By exploring clumpiness as a function of smoothing scale, we find distinct behaviours depending on the method adopted. With Methods #1 and #2, small-scale structures (highlighted by smoothing kernels $\lesssim 50$ pc) show generally low clumpiness values and an anti-correlation with AGN luminosity. At larger smoothing scales ($\gtrsim 80$ pc), clumpiness remains roughly constant with AGN luminosity up to $L_X \approx 10^{42}$ erg s⁻¹, followed by a clear drop at higher luminosities. This behaviour may suggest that larger molecular structures (~ 80 – 100 pc) are more resilient to moderate AGN feedback (as traced by L_X), but are eventually disrupted when the AGN becomes sufficiently powerful.

In contrast, Method #3 consistently reveals a statistically significant breakpoint around $L_X \approx 10^{42}$ erg s⁻¹, even at the smallest scales (~ 30 pc). This indicates that, regardless of the physical scale probed, the fraction of emission associated with compact clumps decreases sharply once the AGN reaches high luminosities. Such behaviour supports the idea that AGN activity can impact both small ($\lesssim 50$ pc) and large ($\gtrsim 80$ pc) molecular structures, potentially through a combination of X-ray irradiation, winds, and cosmic rays.

The different emergence of the breakpoint between Methods #2 and #3 likely reflects the stronger sensitivity of Method #2 to the contrast between clumps and background. At small smoothing scales, more luminous AGNs seem to reduce this contrast, leading to lower values of Σ_{I-B} . Method #3, which does not subtract the background, is less affected and therefore reveals the breakpoint already at small scales. At larger smoothing (≥ 60 pc), the background level decreases and the contrast naturally diminishes, causing the two methods to converge.

The observed flat regime followed by a decline in clumpiness at $L_X \approx 10^{42}$ erg s⁻¹, could be the result of a balance between significant gas inflow from the outer regions (driven by gravitational torque, see e.g. [García-Burillo et al. 2005](#); [Casasola et al. 2008](#); [Combes et al. 2014](#); [Querejeta et al. 2016a](#); [Audibert et al. 2019, 2021](#)) and the mild AGN feedback acting on molecular gas in galaxies below the luminosity breakpoint. In this scenario, the nuclear regions (within 50 pc from the AGN) would maintain

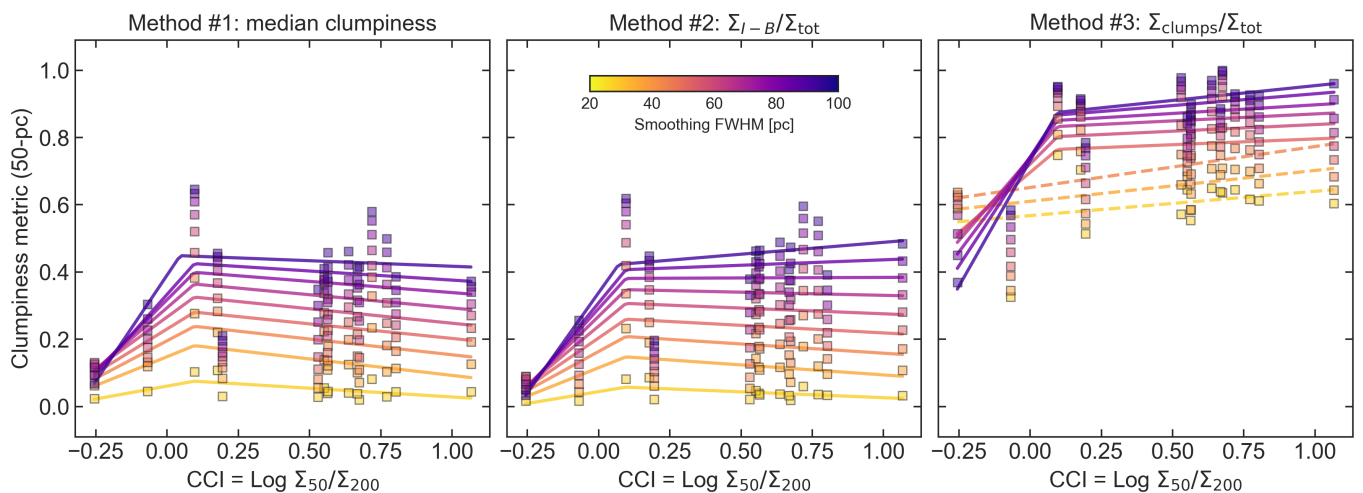


Fig. 5: Clumpiness measured within the 50-pc-radius aperture, plotted as a function of cold molecular gas concentration index (CCI $\equiv \log(\Sigma_{50}/\Sigma_{200})$), where Σ_r is the surface density within an aperture of radius r parsec. Panels, lines, and markers are as in Figure 2.

their clumpiness up to a certain AGN luminosity thanks to the continuous feeding of fresh molecular material, until feedback becomes strong enough to dominate and disperse also the larger molecular complexes.

We note that the three methods we developed to quantify clumpiness, despite being sensitive to different systematics, consistently reveal the same negative trend with L_X . This agreement strengthens the robustness of our finding that higher AGN luminosity is associated with smoother gas distributions.

Interestingly, when measuring clumpiness in the larger aperture (200 pc radius, Figure 4), we do not observe the same turnover: instead, we find a continuous anti-correlation with AGN luminosity, independently of the smoothing kernel size. This may be because, in the larger aperture, we lose the direct view of the nuclear clumpiness and instead average over a broader region of the circumnuclear disk. In this larger region, the inflow of molecular gas at low L_X may be not sufficient to balance the AGN feedback at any of the smoothing scales considered, resulting in a continuous anti-correlation between clumpiness and AGN luminosity. It is also worth noting that, in this larger aperture, the results for some galaxies may be affected by higher noise levels, which can bias the clumpiness measurement. Furthermore, when we isolate the annular region between 50 and 200 pc to exclude the very nucleus, the anti-correlation with AGN luminosity nearly disappears (see Figure A.6), suggesting that the observed trend is mostly driven by the nuclear region itself.

The clumpiness measured in the central 50 pc could in principle reflect the efficiency of AGN feeding: our analysis indeed shows a significant correlation (especially with Methods #1 and #3) with the AGN Eddington ratio λ_{Edd} (Figure A.5). This may suggest that the small-scale molecular gas structure is impacted not only by the AGN radiative power traced by L_X , that is, by the number of high-energy photons, but also by the shape of the spectral energy distribution and/or the black hole mass, both of which influence λ_{Edd} .

5.3. Clumpiness as a function of gas concentration

Our analysis of the molecular gas clumpiness within the central 50 pc shows complex behaviour when compared to the cold molecular gas concentration index (CCI), which quantifies the

radial concentration of molecular gas between 50 and 200 pc scales (see Figure 5). At any smoothing scale, clumpiness seems to be correlated with CCI, with a breakpoint around CCI ~ 0.1 . The absence of a 1:1 correlation imply that other hidden variables, likely including AGN luminosity and feedback processes, also influence gas morphology. Notably, in the clumpiness ratio vs. CCI plot presented in Figure A.8, a similar correlation emerges with a breakpoint around CCI ~ 0.6 , close to the breakpoint found in the CCI vs. L_X plot by García-Burillo et al. (2024).

We note that a correlation between clumpiness and concentration was also reported by Conelice (2003) for stellar light emission on kpc scales: in their case, clumpiness correlated with H α emission from young stars, while concentration was linked to the bulge-to-total light ratio. In our study, these quantities are measured from molecular gas emission within the nuclear 400 pc. Nonetheless, the observed structural change in the molecular gas — from a clumpier to a smoother distribution with increasing AGN luminosity — may have important implications for the host galaxy. A smoother gas distribution could indicate the suppression of dense molecular clouds, thereby reducing the local star formation rate, and at the same time make the gas more vulnerable to being entrained and expelled by AGN-driven winds (see, e.g., Ward et al. 2024). At lower L_X , on the other hand, the higher degree of clumpiness may negatively affect the propagation of jets and winds, causing them to scatter and dissipate their kinetic energy more efficiently into the surrounding ISM (Perucho & Bosch-Ramon 2012; Wagner et al. 2012; Mukherjee et al. 2018; Tanner & Weaver 2022).

6. Conclusions

In this paper, we investigate several methods for measuring the clumpiness of the cold molecular gas in the nuclear region (50 – 200 pc) of galaxies, and its relationship with AGN activity, as measured by the X-ray 2 – 10 keV luminosity L_X , and with cold molecular gas concentration, measured by the index CCI $\equiv \log(\Sigma_{50}/\Sigma_{200})$.

By analysing how clumpiness changes with smoothing scale, we find that small-scale molecular structures (revealed by smoothing $\lesssim 50$ pc) generally show lower clumpiness values and an anti-correlation with AGN luminosity across the entire range of L_X considered (see Figure 2). In contrast, when probing

larger molecular structures ($\sim 70 - 100$ pc) — or when estimating clumpiness more directly, by summing over the clumps without subtracting the underlying background emission — we observe a different behaviour: clumpiness remains roughly constant up to a threshold luminosity of $L_X \approx 10^{42}$ erg s $^{-1}$, beyond which it drops sharply (see Figure 3). This suggests that larger gas clumps may resist AGN feedback at moderate luminosities, possibly due to ongoing inflow that replenishes the nuclear region, but are eventually disrupted at higher AGN power. When measuring clumpiness in the larger 400-pc aperture, however, this turnover effect is not observed: we instead find a continuous anti-correlation with L_X . We also find evidence for a correlation between clumpiness and concentration (CCI), particularly at low CCI values (CCI < 0), while at higher CCI the relation becomes weaker and consistent with a plateau (see Figure 5).

Our interpretation is that AGN feedback partially destroys nuclear molecular gas (hence decreasing its concentration; García-Burillo et al. 2021, 2024), and smooths the surviving clouds, resulting in a less clumpy medium. We interpret this as evidence of negative AGN feedback in the immediate surroundings of the AGN, where the gas becomes less capable of aggregating into dense clouds — a necessary condition for star formation.

It is worth noting that these results were made possible by the high spatial resolution (16 pc) of the gas observations, which allow us to probe the molecular gas in unprecedented detail. In contrast, hydrodynamical simulations still face challenges in capturing the full complexity of the molecular ISM, particularly in modelling the interaction between AGN winds and a clumpy medium, due to the coexistence of vastly different physical scales and gas phases (e.g. McCourt et al. 2018; Meenakshi et al. 2022; Ward et al. 2024).

The results presented here not only reveal a negative correlation between clumpiness and AGN activity, but also highlight the distinct impact of AGN feedback on gas structures at small spatial scales, an aspect that has been poorly investigated in previous studies. As clumpiness becomes an increasingly important parameter for characterising both nearby (Leroy et al. 2013; Sun et al. 2022; Yamamoto et al. 2025) and distant galaxies (Murata et al. 2014; Sok et al. 2025), our analysis offers a complementary perspective on how AGN activity may shape the internal structure of the molecular gas.

Acknowledgements. We thank the anonymous referee for suggestions and comments that helped to improve the presentation of this work. We acknowledge the use of Python (Van Rossum & Drake 2009) and the following libraries: Astropy (Astropy Collaboration et al. 2013, 2018), Matplotlib (Hunter 2007), NumPy (Harris et al. 2020), Pandas (pandas development team 2020), Photutils (Bradley et al. 2024), pwlf (Jekel & Venter 2019), Seaborn (Waskom 2021), and SciPy (Virtanen et al. 2020). This paper makes use of the following ALMA data: ADS/JAO.ALMA#2015.0.00404.S, #2016.1.00254.S, #2016.0.00296.S, #2017.1.00082.S, and #2018.1.00113.S. ALMA is a partnership of ESO (representing its member states), NSF (USA) and NINS (Japan), together with NRC (Canada), MOST and ASIAA (Taiwan), and KASI (Republic of Korea), in cooperation with the Republic of Chile. The Joint ALMA Observatory is operated by ESO, AUI/NRAO and NAOJ. This research has made use of the NASA/IPAC Extragalactic Database (NED), which is funded by the National Aeronautics and Space Administration and operated by the California Institute of Technology. FE acknowledges support from ESA through the Science Faculty - Funding reference ESA-SCI-E-LE-092. FE, SGB, MQ, and AU acknowledge support from the Spanish grant PID2022-138560NB-I00, funded by MCIN/AEI/10.13039/501100011033/FEDER, EU. AAH acknowledges support from grant PID2021-124665NB-I00 funded by MCIN/AEI/10.13039/501100011033 and by ERDF A way of making Europe. AA acknowledges funding from the European Union grant WIDERA ExGal-Twin, GA 101158446. AJB acknowledges funding from the “FirstGalaxies” Advanced Grant from the European Research Council (ERC) under the European Union’s Horizon 2020 research and innovation program (Grant agreement No. 789056). CRA and AA acknowledge support from project “Track-

ing active galactic nuclei feedback from parsec to kiloparsec scales”, with reference PID2022-141105NB-I00. EB acknowledges support from the Spanish grants PID2022-138621NB-I00 and PID2021-123417OB-I00, funded by MCIN/AEI/10.13039/501100011033/FEDER, EU. IGB is supported by the Programa Atracción de Talento Investigador “César Nombela” via grant 2023-T1/TEC-29030 funded by the Community of Madrid. OGM acknowledge financial support for PAPIIT/UNAM project IN1097123 and Ciencia de Frontera (SECIHTI) project CF-2023-G100. SFH acknowledges support through UK Research and Innovation (UKRI) under the UK government’s Horizon Europe funding Guarantee (EP/Z533920/1) and an STFC Small Award (ST/Y001656/1).

References

- Alonso-Herrero, A., García-Burillo, S., Hönic, S. F., et al. 2021, *A&A*, 652, A99
 Astropy Collaboration, Price-Whelan, A. M., Sipőcz, B. M., et al. 2018, *AJ*, 156, 123
 Astropy Collaboration, Robitaille, T. P., Tollerud, E. J., et al. 2013, *A&A*, 558, A33
 Audibert, A., Combes, F., García-Burillo, S., et al. 2019, *A&A*, 632, A33
 Audibert, A., Combes, F., García-Burillo, S., et al. 2021, *A&A*, 656, A60
 Baumgartner, W. H., Tueller, J., Markwardt, C. B., et al. 2013, *ApJS*, 207, 19
 Bergin, E. A. & Tafalla, M. 2007, *ARA&A*, 45, 339
 Bertola, E., Circosta, C., Ginolfi, M., et al. 2024, *A&A*, 691, A178
 Bessiere, P. S. & Ramos Almeida, C. 2022, *MNRAS*, 512, L54
 Bischetti, M., Maiolino, R., Carniani, S., et al. 2019, *A&A*, 630, A59
 Bolatto, A. D., Wolfire, M., & Leroy, A. K. 2013, *ARA&A*, 51, 207
 Bradley, L., Sipőcz, B., Robitaille, T., et al. 2024, *astropy/photutils: 2.0.2*
 Buck, T., Pfrommer, C., Girichidis, P., & Corobean, B. 2022, *MNRAS*, 513, 1414
 Carniani, S., Marconi, A., Maiolino, R., et al. 2017, *A&A*, 605, A105
 Casasola, V., Combes, F., García-Burillo, S., et al. 2008, *A&A*, 490, 61
 Chevance, M., Kruijssen, J. M. D., Vazquez-Semadeni, E., et al. 2020, *Space Sci. Rev.*, 216, 50
 Chevance, M., Krumholz, M. R., McLeod, A. F., et al. 2023, in *Astronomical Society of the Pacific Conference Series*, Vol. 534, *Protostars and Planets VII*, ed. S. Inutsuka, Y. Aikawa, T. Muto, K. Tomida, & M. Tamura, 1
 Cicone, C., Maiolino, R., Sturm, E., et al. 2014, *A&A*, 562, A21
 Circosta, C., Mainieri, V., Lamperti, I., et al. 2021, *A&A*, 646, A96
 Combes, F., García-Burillo, S., Audibert, A., et al. 2019, *A&A*, 623, A79
 Combes, F., García-Burillo, S., Casasola, V., et al. 2014, *A&A*, 565, A97
 Conzelmann, C. J. 2003, *ApJS*, 147, 1
 Crutcher, R. M. 2012, *ARA&A*, 50, 29
 Elia, D., Strafella, F., Dib, S., et al. 2018, *MNRAS*, 481, 509
 Ellison, S. L., Wong, T., Sánchez, S. F., et al. 2021, *MNRAS*, 505, L46
 Elmegreen, B. G. & Falgarone, E. 1996, *ApJ*, 471, 816
 Esposito, F., Alonso-Herrero, A., García-Burillo, S., et al. 2024a, *A&A*, 686, A46
 Esposito, F., Vallini, L., Pozzi, F., et al. 2024b, *MNRAS*, 527, 8727
 Esposito, F., Vallini, L., Pozzi, F., et al. 2022, *MNRAS*, 512, 686
 Fabian, A. C. 2012, *ARA&A*, 50, 455
 Faucher-Giguère, C.-A. & Quataert, E. 2012, *MNRAS*, 425, 605
 Federrath, C. & Klessen, R. S. 2012, *ApJ*, 761, 156
 Fiore, F., Feruglio, C., Shankar, F., et al. 2017, *A&A*, 601, A143
 Fluetsch, A., Maiolino, R., Carniani, S., et al. 2019, *MNRAS*, 483, 4586
 Francis, L., Johnstone, D., Herczeg, G., Hunter, T. R., & Harsono, D. 2020, *AJ*, 160, 270
 Fukui, Y. & Kawamura, A. 2010, *ARA&A*, 48, 547
 Fuller, L., Lopez-Rodriguez, E., García-Bernete, I., et al. 2025, *ApJS*, 276, 64
 Gabici, S. 2022, *A&A Rev.*, 30, 4
 García, P., Bronfman, L., Nyman, L.-Å., Dame, T. M., & Luna, A. 2014, *ApJS*, 212, 2
 García-Bernete, I., Alonso-Herrero, A., García-Burillo, S., et al. 2021, *A&A*, 645, A21
 García-Bernete, I., Alonso-Herrero, A., Rigopoulou, D., et al. 2024a, *A&A*, 681, L7
 García-Bernete, I., Rigopoulou, D., Donnan, F. R., et al. 2024b, *A&A*, 691, A162
 García-Burillo, S., Alonso-Herrero, A., Ramos Almeida, C., et al. 2021, *A&A*, 652, A98
 García-Burillo, S., Combes, F., Schinnerer, E., Boone, F., & Hunt, L. K. 2005, *A&A*, 441, 1011
 García-Burillo, S., Hicks, E. K. S., Alonso-Herrero, A., et al. 2024, *A&A*, 689, A347
 Genzel, R., Förster Schreiber, N. M., Rosario, D., et al. 2014, *ApJ*, 796, 7
 Harris, C. R., Millman, K. J., van der Walt, S. J., et al. 2020, *Nature*, 585, 587
 Harrison, C. M., Costa, T., Tadhunter, C. N., et al. 2018, *Nature Astronomy*, 2, 198
 Harrison, C. M. & Ramos Almeida, C. 2024, *Galaxies*, 12, 17
 Heckman, T. M. & Best, P. N. 2014, *ARA&A*, 52, 589

- Heyer, M. & Dame, T. M. 2015, *ARA&A*, 53, 583
- Hunter, J. D. 2007, *Computing in Science & Engineering*, 9, 90
- Israel, F. P. 2020, *A&A*, 635, A131
- Jekel, C. F. & Venter, G. 2019, *pwlif: A Python Library for Fitting 1D Continuous Piecewise Linear Functions*
- Kormendy, J. & Ho, L. C. 2013, *ARA&A*, 51, 511
- Koss, M., Trakhtenbrot, B., Ricci, C., et al. 2017, *ApJ*, 850, 74
- Koutsoumpou, E., Fernández-Ontiveros, J. A., Dasyra, K. M., & Spinoglio, L. 2025, *A&A*, 693, A215
- Krajnović, D., Cappellari, M., de Zeeuw, P. T., & Copin, Y. 2006, *MNRAS*, 366, 787
- Krumholz, M. R. 2014, *Phys. Rep.*, 539, 49
- Krumholz, M. R., McKee, C. F., & Bland-Hawthorn, J. 2019, *ARA&A*, 57, 227
- Leroy, A. K., Lee, C., Schrupa, A., et al. 2013, *ApJ*, 769, L12
- Leroy, A. K., Schinnerer, E., Hughes, A., et al. 2021, *ApJS*, 257, 43
- Maiolino, R., Gallerani, S., Neri, R., et al. 2012, *MNRAS*, 425, L66
- Maiolino, R., Russell, H. R., Fabian, A. C., et al. 2017, *Nature*, 544, 202
- Maloney, P. R., Hollenbach, D. J., & Tielens, A. G. G. M. 1996, *ApJ*, 466, 561
- Massi, F., Weiss, A., Elia, D., et al. 2019, *A&A*, 628, A110
- McCourt, M., Oh, S. P., O’Leary, R., & Madigan, A.-M. 2018, *MNRAS*, 473, 5407
- McKee, C. F. & Ostriker, E. C. 2007, *ARA&A*, 45, 565
- Meenakshi, M., Mukherjee, D., Wagner, A. Y., et al. 2022, *MNRAS*, 516, 766
- Mercedes-Feliz, J., Anglés-Alcázar, D., Hayward, C. C., et al. 2023, *MNRAS*, 524, 3446
- Mingozzi, M., Vallini, L., Pozzi, F., et al. 2018, *MNRAS*, 474, 3640
- Morganti, R. 2017, *Frontiers in Astronomy and Space Sciences*, 4, 42
- Mukherjee, D., Bicknell, G. V., Wagner, A. Y., Sutherland, R. S., & Silk, J. 2018, *MNRAS*, 479, 5544
- Murata, K. L., Kajisawa, M., Taniguchi, Y., et al. 2014, *ApJ*, 786, 15
- Namekata, D., Umemura, M., & Hasegawa, K. 2014, *MNRAS*, 443, 2018
- Nims, J., Quataert, E., & Faucher-Giguère, C.-A. 2015, *MNRAS*, 447, 3612
- Omont, A. 2007, *Reports on Progress in Physics*, 70, 1099
- pandas development team, T. 2020, *pandas-dev/pandas: Pandas*
- Perucho, M. & Bosch-Ramon, V. 2012, *A&A*, 539, A57
- Petrosian, V. 1976, *ApJ*, 210, L53
- Pier, E. A. & Voit, G. M. 1995, *ApJ*, 450, 628
- Poitevineau, R., Combes, F., García-Burillo, S., et al. 2025, *A&A*, 693, A311
- Pozzi, F., Vallini, L., Vignali, C., et al. 2017, *MNRAS*, 470, L64
- Querejeta, M., Meidt, S. E., Schinnerer, E., et al. 2016a, *A&A*, 588, A33
- Querejeta, M., Schinnerer, E., García-Burillo, S., et al. 2016b, *A&A*, 593, A118
- Ramos Almeida, C., Bischetti, M., García-Burillo, S., et al. 2022, *A&A*, 658, A155
- Ricci, C., Trakhtenbrot, B., Koss, M. J., et al. 2017, *ApJS*, 233, 17
- Rosario, D. J., Togi, A., Burtscher, L., et al. 2019, *ApJ*, 875, L8
- Sabatini, G., Gruppioni, C., Massardi, M., et al. 2018, *MNRAS*, 476, 5417
- Schartmann, M., Krause, M., & Burkert, A. 2011, *MNRAS*, 415, 741
- Sok, V., Muzzin, A., Jablonka, P., et al. 2025, *ApJ*, 979, 14
- Solomon, P. M., Rivolo, A. R., Barrett, J., & Yahil, A. 1987, *ApJ*, 319, 730
- Sun, J., Leroy, A. K., Rosolowsky, E., et al. 2022, *AJ*, 164, 43
- Tadaki, K., Esposito, F., Vallini, L., et al. 2025, *Nature Astronomy*, 9, 720
- Tanner, R. & Weaver, K. A. 2022, *AJ*, 163, 134
- Vallini, L., Ferrara, A., Pallottini, A., & Gallerani, S. 2017, *MNRAS*, 467, 1300
- Van Rossum, G. & Drake, F. L. 2009, *Python 3 Reference Manual* (Scotts Valley, CA: CreateSpace)
- Virtanen, P., Gommers, R., Oliphant, T. E., et al. 2020, *Nature Methods*, 17, 261
- Viti, S., García-Burillo, S., Fuente, A., et al. 2014, *A&A*, 570, A28
- Wagner, A. Y., Bicknell, G. V., & Umemura, M. 2012, *ApJ*, 757, 136
- Ward, S. R., Costa, T., Harrison, C. M., & Mainieri, V. 2024, *MNRAS*, 533, 1733
- Waskom, M. L. 2021, *Journal of Open Source Software*, 6, 3021
- Wolfire, M. G., Vallini, L., & Chevance, M. 2022, *ARA&A*, 60, 247
- Yamamoto, T., Iono, D., Saito, T., et al. 2025, *PASJ*, 77, 288
- Zhang, L., Packham, C., Hicks, E. K. S., et al. 2024, *ApJ*, 974, 195
- ⁷ Kavli Institute for Particle Astrophysics & Cosmology (KIPAC), Stanford University, Stanford, CA 94305, USA
- ⁸ Instituto de Radioastronomía y Astrofísica (IRyA-UNAM), Antigua Carretera a Pátzcuaro #8701, Ex-Hda. San José de la Huerta, C.P. 58089, Morelia, Michoacán, Mexico
- ⁹ Instituto de Astrofísica de Canarias (IAC), Calle Vía Láctea, s/n, 38205 La Laguna, Tenerife, Spain
- ¹⁰ Departamento de Astrofísica, Universidad de La Laguna, 38206 La Laguna, Tenerife, Spain
- ¹¹ Department of Physics & Astronomy, University of Alaska Anchorage, Anchorage, AK, 99508-4664, USA
- ¹² Department of Astronomy, University of Geneva, 1290 Versoix, Switzerland
- ¹³ Instituto de Estudios Astrofísicos, Facultad de Ingeniería y Ciencias, Universidad Diego Portales, Av. Ejército Libertador 441, Santiago, Chile
- ¹⁴ Departamento de Física de la Tierra y Astrofísica, Fac. de CC. Físicas, Universidad Complutense de Madrid, 28040 Madrid, Spain
- ¹⁵ Instituto de Física de Partículas y del Cosmos IPARCOS, Universidad Complutense de Madrid, 28040 Madrid, Spain
- ¹⁶ Cahill Center for Astrophysics, California Institute of Technology, 1216 East California Boulevard, Pasadena, CA 91125, USA
- ¹⁷ Department of Physics, University of Oxford, Denys Wilkinson Building, Keble Road, Oxford, OX13RH, UK
- ¹⁸ School of Mathematics, Statistics and Physics, Newcastle University, Newcastle upon Tyne, NE1 7RU, UK
- ¹⁹ Institute of Astrophysics, Foundation for Research and Technology – Hellas (FORTH), Voutes 70013, Heraklion, Greece
- ²⁰ School of Sciences, European University Cyprus, Diogenes street, Engomi 1516 Nicosia, Cyprus
- ²¹ School of Physics & Astronomy, University of Southampton, Southampton, SO17 1BJ, Hampshire, UK
- ²² Telespazio UK for the European Space Agency (ESA), ESAC, Camino Bajo del Castillo s/n, 28692 Villanueva de la Cañada, Madrid, Spain
- ²³ Space Telescope Science Institute, 3700 San Martin Drive Baltimore, MD 21218, USA
- ²⁴ Department of Physics and Astronomy, The University of Texas at San Antonio, 1 UTSA Circle, San Antonio, TX 78249, USA
- ²⁵ Instituto de Física Fundamental, CSIC, Calle Serrano 123, 28006, Madrid, Spain
- ²⁶ Centro de Astrobiología (CAB, CSIC/INTA), Ctra de Torrejón a Ajalvir, km 4, 28850 Torrejón de Ardoz, Madrid, Spain
- ²⁷ Departamento de Física, CCNE, Universidade Federal de Santa Maria, Av. Roraima 1000, 97105-900, Santa Maria, RS, Brazil

¹ Observatorio de Madrid, OAN-IGN, Alfonso XII, 3, E-28014 Madrid, Spain

e-mail: f.esposito@oan.es

² Centro de Astrobiología (CAB, CSIC-INTA), Camino Bajo del Castillo s/n, E-28692 Villanueva de la Cañada, Madrid, Spain

³ Observatoire de Paris, LUX, PSL University, Sorbonne Université, CNRS, F-75014 Paris, France

⁴ Collège de France, 11 Place Marcelin Berthelot, 75231 Paris, France

⁵ Max-Planck-Institut für Extraterrestrische Physik, Postfach 1312, 85741, Garching, Germany

⁶ Department of Physics & Astronomy, University of South Carolina, Columbia, SC 29208, USA

Appendix A: Ancillary material: sensitivities, emission maps, clumpiness analysis, and additional correlations

In this appendix we present the main ancillary information and visual material used in this study. Table A.1 lists the basic properties of the 16 galaxies analysed: equatorial coordinates, luminosity distances, hard X-ray luminosity (L_X), Eddington ratios (λ_{Edd}), inclinations, and position angles.

Figure A.1 shows the RMS sensitivity (in $\text{Jy km s}^{-1} \text{beam}^{-1}$) as a function of luminosity distance, demonstrating that there is no correlation between the two. Figure A.2 presents the same sensitivities converted into molecular mass surface densities ($M_\odot \text{pc}^{-2}$), using the conversion factors discussed in Section 2. In addition, we show the ALMA CO(3–2) integrated intensity maps (moment 0) of the sample (Figure A.3).

For four representative galaxies, we present the clumpiness maps computed at different smoothing scales (Figure A.4). The galaxies are selected to cover the L_X range: NGC 1326 ($L_X = 10^{39.9} \text{ erg s}^{-1}$), NGC 6300 ($L_X = 10^{41.7} \text{ erg s}^{-1}$), NGC 3227 ($L_X = 10^{42.4} \text{ erg s}^{-1}$), and NGC 7582 ($L_X = 10^{43.5} \text{ erg s}^{-1}$). These maps illustrate how the choice of smoothing kernel highlights structures of different sizes and contrast in the molecular gas distribution.

We also present additional tests and correlations to complement the main results described in Section 4. Specifically, we explore how clumpiness varies with the Eddington ratio (Figure A.5), when measured in an annular region excluding the nucleus (Figure A.6), and how the ratio of nuclear to circumnuclear clumpiness depends on AGN luminosity and molecular gas concentration (Figures A.7 and A.8).

Table A.1: Properties of the sample.

Name	D_L	$\log L_X^{2-10 \text{ keV}}$	$\log \lambda_{\text{Edd}}$	i	PA
	Mpc	erg s^{-1}		°	°
NGC 613	17.2	41.20	-3.48	36	122
NGC 1068	14.0	42.82	-0.70	41	289
NGC 1326	14.9	39.90	-4.02	53	71
NGC 1365	18.3	42.09	-2.15	41	40
NGC 1433	9.7	39.20	–	33	199
NGC 1566	7.2	40.50	-2.89	49	44
NGC 1672	11.4	39.10	-6.41	29	155
NGC 3227	23.0	42.37	-1.20	52	152
NGC 4941	20.5	41.40	-2.10	41	212
NGC 5643	16.9	42.41	-1.23	30	301
NGC 6300	14.0	41.73	-1.72	57	95
NGC 6814	22.8	42.24	-1.62	57	84
NGC 7213	22.0	41.85	-3.01	35	133
NGC 7314	17.4	42.18	-2.07	55	191
NGC 7465	27.2	41.93	-2.10	54	66
NGC 7582	22.5	43.49	-1.70	59	344

Notes. Distances (D_L) are median values of redshift-independent distances taken from the Nasa Extragalactic Database (NED). X-ray luminosities ($L_X^{2-10 \text{ keV}}$) are taken from Ricci et al. (2017); Combes et al. (2019); García-Burillo et al. (2024). Eddington ratios (λ_{Edd}) are taken from Koss et al. (2017); García-Burillo et al. (2024). Inclinations (i) and position angles (PA) were derived with the kinemetry software (Krajinović et al. 2006) as presented in García-Burillo et al. (2021).

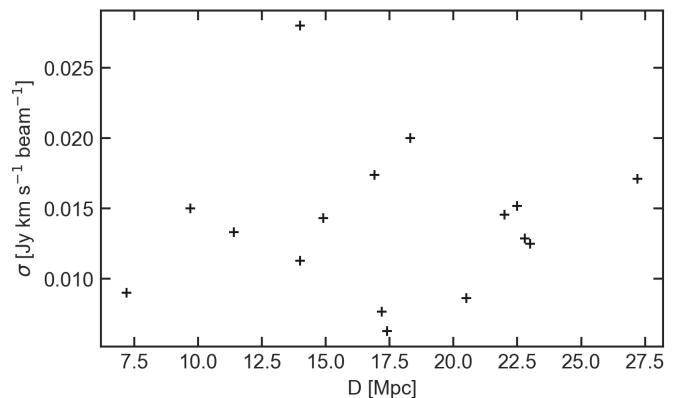


Fig. A.1: RMS sensitivities (σ) of the CO(3–2) maps in units of $\text{Jy km s}^{-1} \text{beam}^{-1}$ as a function of luminosity distance (in Mpc). No correlation is found between sensitivity and distance.

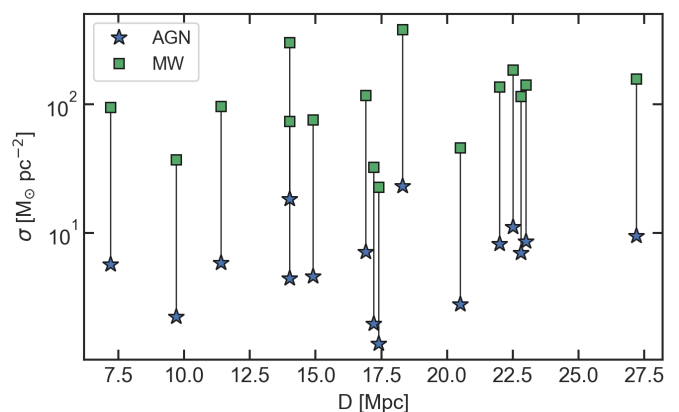


Fig. A.2: RMS sensitivities (σ) of the CO(3–2) maps converted into molecular mass surface densities (in $M_\odot \text{pc}^{-2}$) as a function of luminosity distance (in Mpc). For each galaxy we show two values, connected by a vertical bar: green squares correspond to the case $r_{31} = 0.7$ (average value in galaxy centers, Israel 2020) combined with the standard Milky Way disk conversion factor $X_{\text{CO}} = 2 \times 10^{20} \text{ mol cm}^{-2} (\text{K km s}^{-1})^{-1}$ (Bolatto et al. 2013); blue stars correspond to the case $r_{31} = 2.9$ (measured at the AGN position in NGC 1068, Viti et al. 2014) combined with the recommended conversion factor for the nuclear region of the Milky Way $X_{\text{CO}} = 0.5 \times 10^{20} \text{ mol cm}^{-2} (\text{K km s}^{-1})^{-1}$ (Bolatto et al. 2013).

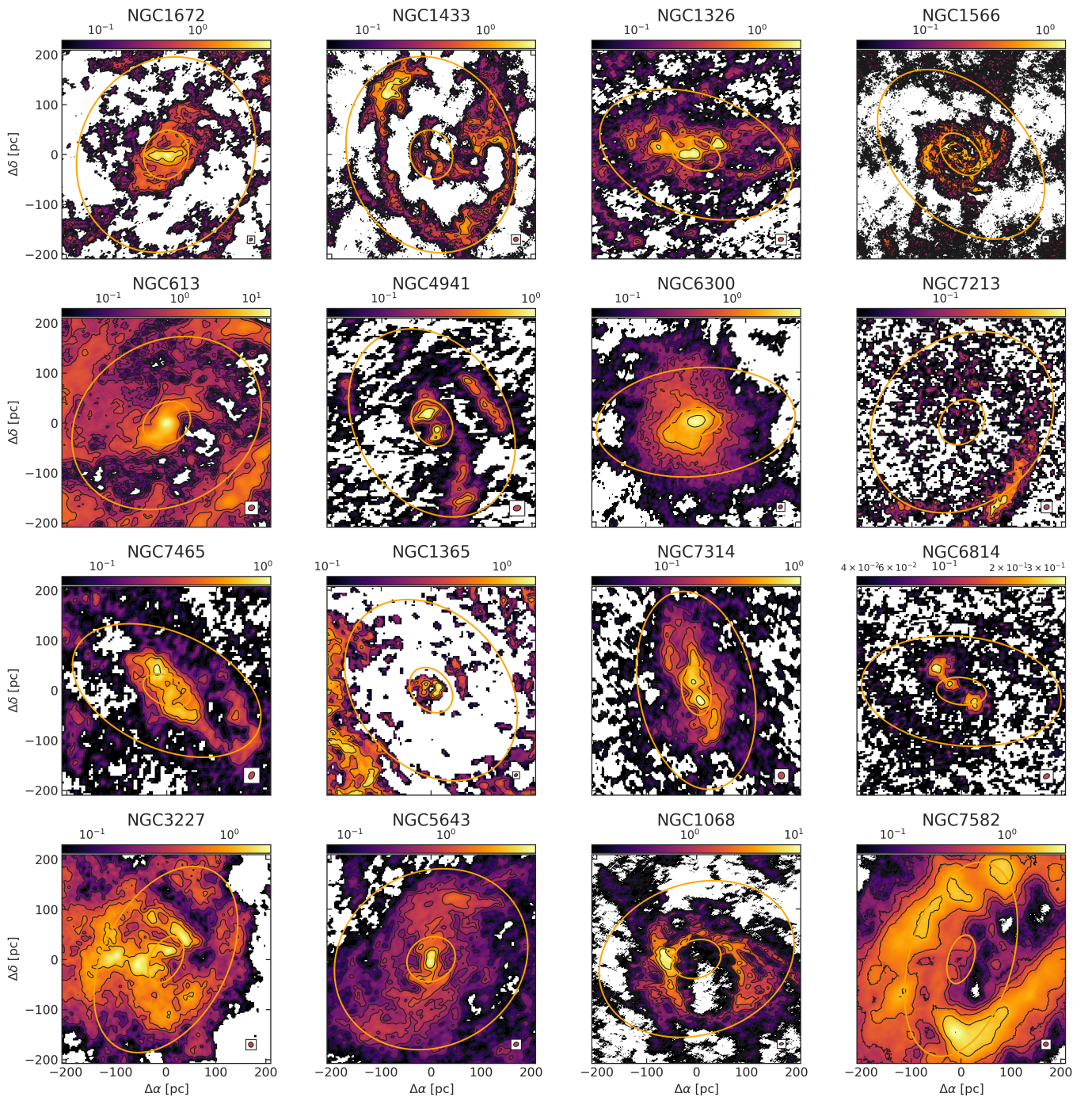


Fig. A.3: CO(3 – 2) images of the sample galaxies. Each image covers a region of $400 \text{ pc} \times 400 \text{ pc}$, as in Figure 1. The two ellipses in each panel correspond to circles with radii of 50 and 200 pc projected onto the plane of the galaxy. Galaxies are ordered by increasing 2 – 10 keV luminosity, from top-left to bottom-right. Contours correspond to $(3, 5, 10, 20, 30, 50, 100, 200) \times \sigma$. The red ellipse inside the white square at the bottom-right corner of each panel represents the ALMA beam.

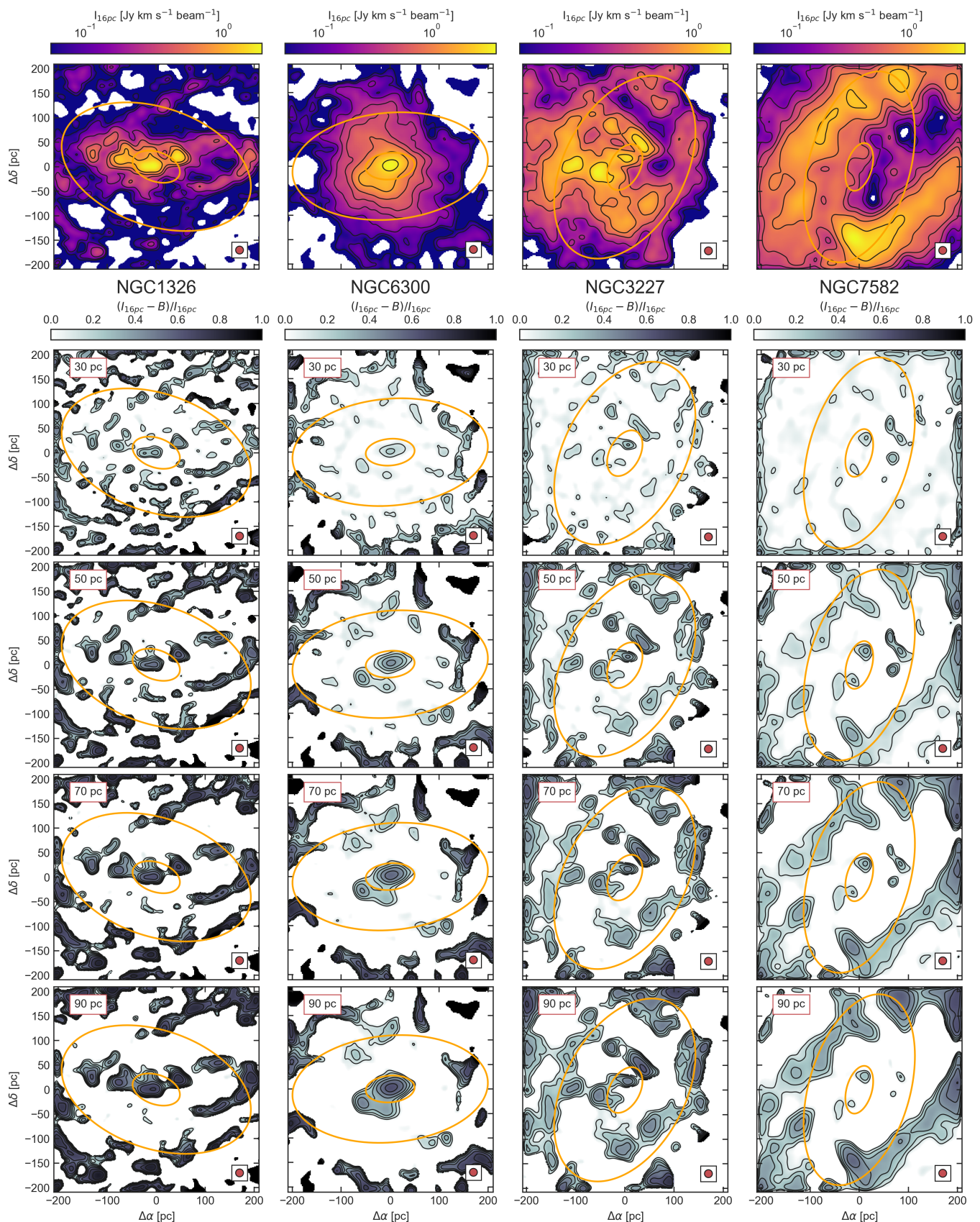


Fig. A.4: CO(3–2) maps smoothed to a common physical resolution of 16 pc for four representative galaxies (*top row*): NGC 1326, NGC 6300, NGC 3227, and NGC 7582 (from left to right). Contours are the same as in Figure A.3. The colourbars indicate flux in $\text{Jy km s}^{-1} \text{beam}^{-1}$. From the second to the fifth row, for each galaxy (each column), we show the clumpiness map computed with Method #1, using Gaussian smoothing kernels with FWHM of 30, 50, 70, and 90 pc (from top to bottom). Contours are plotted every 0.1 between 0 and 1. The two ellipses in each panel correspond to circles with radii of 50 and 200 pc projected onto the plane of the galaxy. The red ellipse inside the white square at the bottom-right corner of each panel represents the ALMA beam.

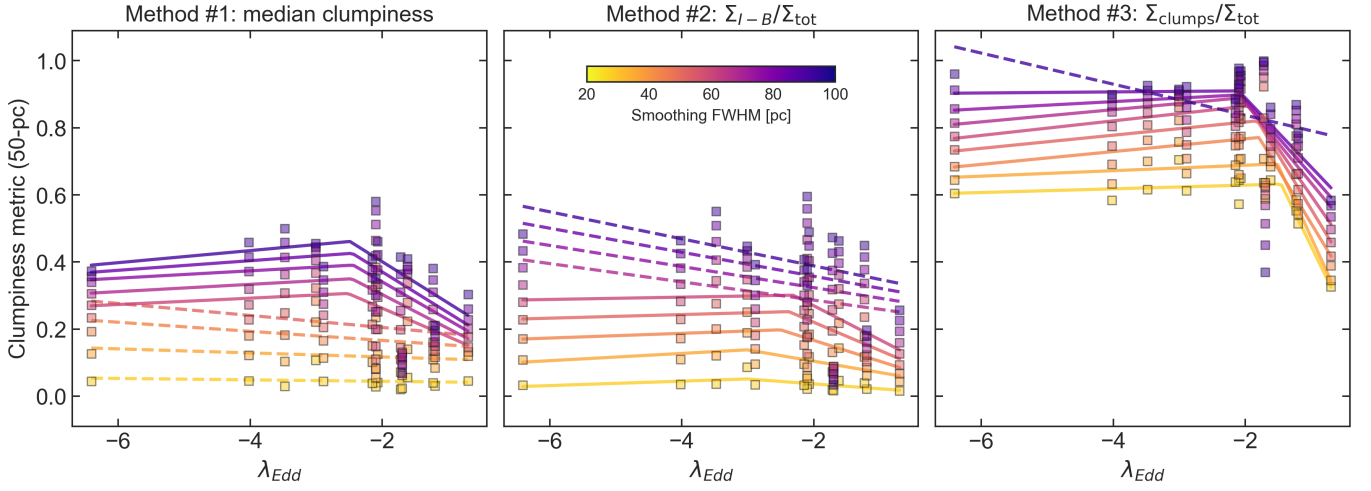


Fig. A.5: Clumpiness measured within the 50-pc-radius aperture, plotted as a function of the AGN Eddington ratio, λ_{Edd} . Panels, lines, and markers are as in Figure 2.

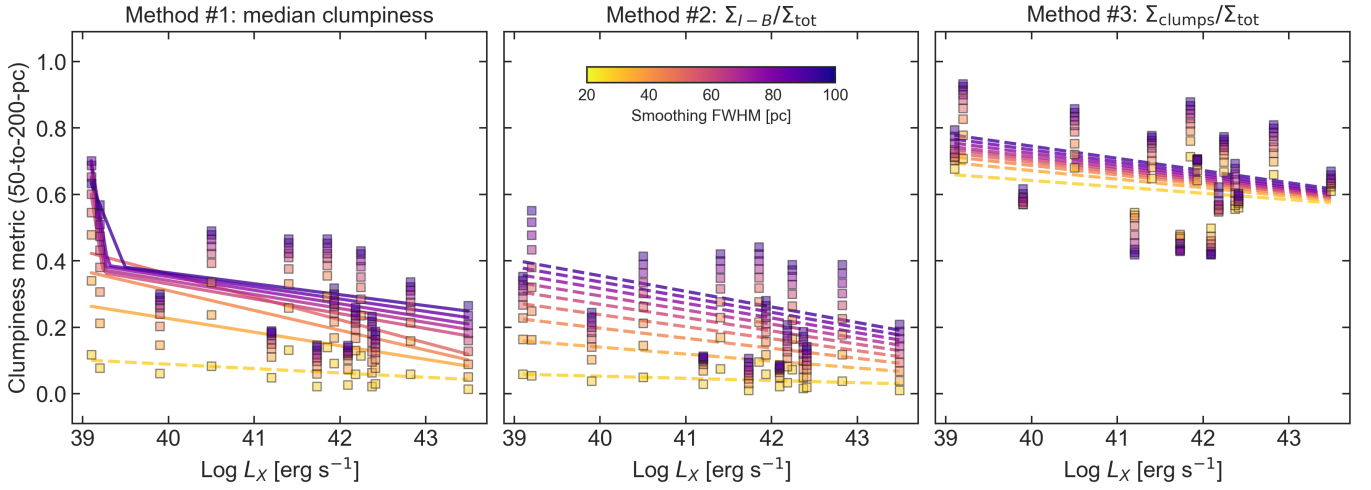


Fig. A.6: Clumpiness measured within the annular aperture between 50 and 200 pc, plotted as a function of AGN X-ray luminosity. Panels, lines, and markers are as in Figure 2.

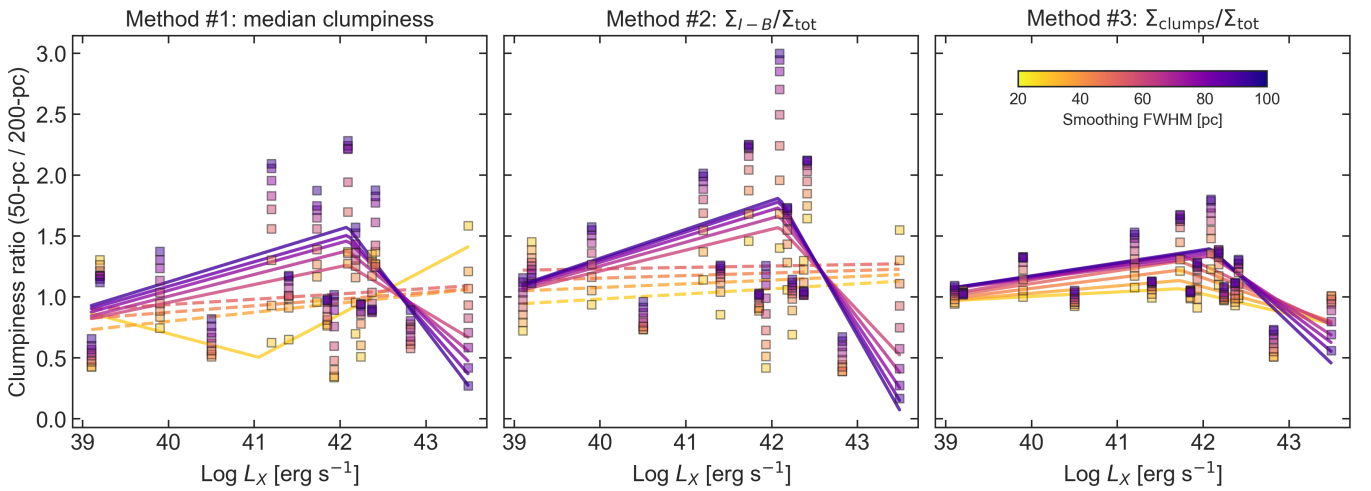


Fig. A.7: Ratio of clumpiness measured within the 50-pc-radius aperture to that measured within the 200-pc-radius aperture, plotted as a function of AGN X-ray luminosity. Panels, lines, and markers are as in Figure 2.

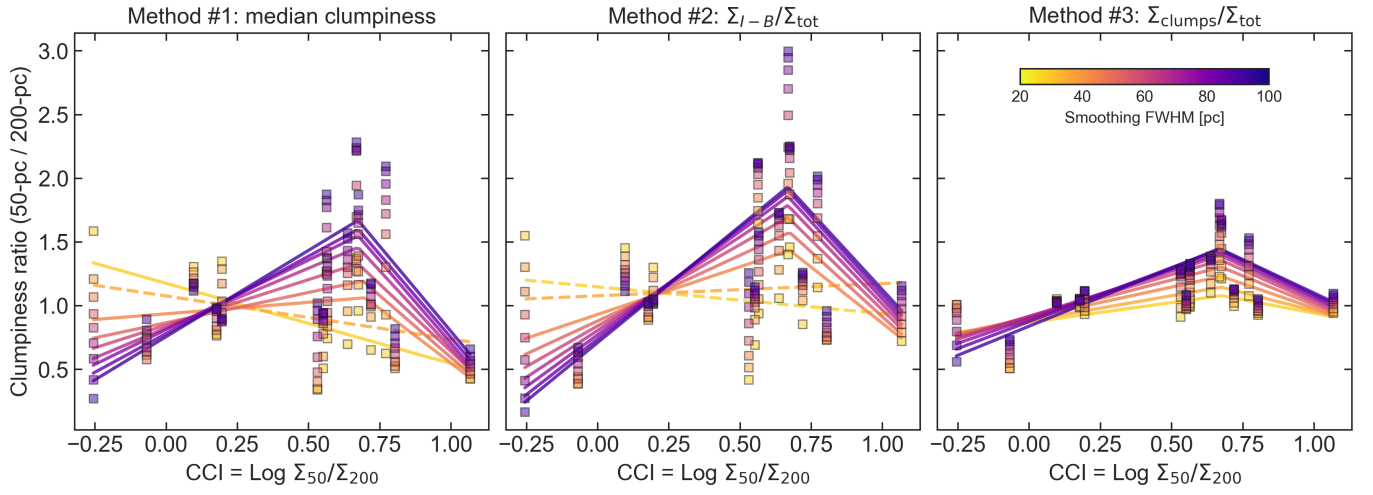


Fig. A.8: Ratio of clumpiness measured within the 50-pc-radius aperture to that within the 200-pc-radius aperture, plotted as a function of the cold molecular gas concentration index, $CCI \equiv \log(\Sigma_{50}/\Sigma_{200})$. Panels, lines, and markers are as in Figure 2.